

Large Tunnel Electroresistance with Ultrathin $\text{Hf}_{0.5}\text{Zr}_{0.5}\text{O}_2$ Ferroelectric Tunnel Barriers

Bhagwati Prasad,* Vishal Thakare, Alan Kalitsov, Zimeng Zhang, Bruce Terris, and Ramamoorthy Ramesh*

Hafnia-based ferroelectric tunnel junctions (FTJs) hold great promise for nonvolatile memory and emerging data storage applications. In this article, a large tunnel electroresistance effect with ultrathin $\text{Hf}_{0.5}\text{Zr}_{0.5}\text{O}_2$ (HZO) barrier based FTJs is reported. Robust ferroelectricity is achieved with ≈ 1 nm films by stabilizing the rhombohedral polar phase of HZO (R-HZO) through a large compressive strain, induced by growing the film epitaxially on a SrTiO_3 (001) substrate. The OFF/ON ratio of the junction resistance at zero bias is about 135 with ≈ 1 nm thick barrier, which increases to $\approx 10^5$ with increasing the barrier thickness to ≈ 2.5 nm. The resistance-area product (RA) of tunnel junctions is reduced by nearly three orders of magnitude by using an ≈ 1 nm R-HZO barrier as compared with typically reported RA values for doped- HfO_2 barrier based FTJs, which significantly improves signal-to-noise ratio during the read operation. These results set the stage for further exploration of Hafnia-based FTJs for non-volatile memory applications.

High density, high-speed, and low power consuming nonvolatile memories are currently being vigorously explored for use in next-generation computation, particularly due to the performance gap between the logic and memory elements of the current computational architecture.^[1–3] Of various explored material systems, electrically switchable spontaneous polarization of ferroelectric materials enables a robust nonvolatile memory solution.^[4–6] One such promising memory element is the ferroelectric tunnel junction (FTJ), which, unlike ferroelectric RAM, offers nondestructive readout, in addition to low operation energy and high operation speed.^[7] In an FTJ,

an ultrathin film of a ferroelectric material, sandwiched between two metallic electrodes having different electronic screening lengths, is used as a tunnel barrier that provides a route to modulate the resistance states of a tunnel device upon the application of an electric field. This so-called tunnel electroresistance (TER) effect, is created by manipulating the polarization states of the barrier layer.^[8,9] In these devices, the bound charges in the form of electric dipole moments in the ferroelectric barrier layer do not fully compensate the electrode charges at barrier/electrode interface due to the limited screening length of electrons in metals. Hence, if the two electrodes have different screening lengths, the potential profile across the barrier layer modulates asymmetrically with the polarization reversal


which thereby will significantly alter the tunneling current.^[9,10]

FTJs with various perovskite ferroelectric barrier materials have been explored extensively in the last decade.^[8,9,11,12] However, due to their limitation in terms of lattice, chemical, and thermal compatibility with traditional complementary metal-oxide-semiconductor (CMOS) processing in addition to scalability issues, FTJ have not attracted much attention from technological viewpoints. In 2011, ferroelectricity was discovered in polycrystalline doped HfO_2 thin films,^[13] which triggered significant interest in ferroelectric memories, including FTJs, mainly due to known integration processes of HfO_2 based thin films with CMOS devices since 1990.^[7] In addition, ferroelectricity in doped HfO_2 can be stabilized easily in polycrystalline ultrathin films by retaining the desired stress state via doping, electrode layers, or annealing process.^[14–17] These factors make the HfO_2 system an appealing candidate for the ferroelectric barrier in FTJs for nonvolatile memory applications. Recently, doped HfO_2 based FTJs have been investigated with ≈ 2 – 4 nm thick barrier,^[18–22] but the tunneling current density of these devices is too small, particularly due to the highly insulating nature of HfO_2 (bandgap ≈ 5 – 6 eV); hence the low signal-to-noise ratio (SNR) during the read operation is still a major issue. Therefore, reducing the thickness of the barrier layer down to 2–3-unit cells is required to enhance the tunneling current density as it depends exponentially on the thickness of the barrier layer. Moreover, obtaining the single-phase ferroelectric films with ALD-grown polycrystalline samples has been challenging.^[14] The presence of oxygen vacancies and defects in

Dr. B. Prasad, Dr. A. Kalitsov, Dr. B. Terris
Western Digital Research Center
Western Digital Corporation
San Jose, CA 95119, USA
E-mail: bhagwati.prasad@wdc.com

Dr. V. Thakare, Z. Zhang, Prof. R. Ramesh
Department of Materials Science and Engineering
University of California
Berkeley, CA 94720, USA
E-mail: rramesh@berkeley.edu

Prof. R. Ramesh
Department of Physics
University of California
Berkeley, CA 94720, USA

 The ORCID identification number(s) for the author(s) of this article can be found under <https://doi.org/10.1002/aelm.202001074>.

DOI: 10.1002/aelm.202001074

these films, particularly at the interfaces diminish the ferroelectricity. Therefore, single-crystalline epitaxial films are desirable for achieving ferroelectricity in ultrathin films.

In this letter, we demonstrate FTJs with a very large OFF/ON resistance ratio and relatively low resistance area product (RA) with ≈ 1 nm thick Zr doped HfO_2 (HZO) ferroelectric tunnel barrier. We stabilized ferroelectricity in ultrathin films of rhombohedral HZO (R-HZO) through the substrate-induced compressive strain by growing the epitaxial films on single crystalline SrTiO_3 (STO) (001) substrates. The resistance area product at the bias voltage (≈ 300 mV) required for one-half of the zero-bias TER ratio is three orders of magnitude lower than the reported value with relatively thick ferroelectric barriers.^[22] The OFF/ON resistance ratio of 135 achieved with ≈ 1 nm barrier, which is enhanced to 10^5 with increasing the barrier thickness to 2.5 nm, is amongst the highest reported values for HZO based FTJs.

The extent of the modulation of the ferroelectric tunnel barrier in FTJs devices depends upon the difference in the screening lengths of electrons in the two opposing electrodes. Typically conducting oxides show one order of magnitude higher electronic screening length than metals and hence a conducting oxide/ferroelectric barrier/ metal structure is commonly used for FTJ devices. In this work, we have used $\text{La}_{0.7}\text{Sr}_{0.3}\text{MnO}_3$ (LSMO) as a bottom oxide electrode for our FTJ devices. LSMO films with a thickness of ≈ 60 nm were first deposited onto a STO (001) substrate, and subsequently, HZO films with varying thicknesses were deposited onto the LSMO seed layer. Pulsed laser deposition (PLD) was employed to deposit these oxide films. The X-ray diffraction patterns (2θ - θ scan) of HZO (1, 2.5, and 10 nm)/LSMO (60 nm) film is shown in Figure 1 (see Figure S1a, Supporting Information for the XRD patterns with several other thicknesses of HZO layer ranging from 1 to 18 nm). The growth rate for these films was first estimated from X-ray reflectivity (XRR) (see Figure S1b, Supporting Information) and later confirmed by transmis-

sion electron microscopy (TEM) (see Figure S1d, Supporting Information) measurements. The intense diffraction peak in the vicinity of the STO (001) peak corresponds to the (001) reflection of LSMO, which indicates epitaxial growth. Typically, the (111) reflection of the orthorhombic phase of HZO films appears around 30.5° ; however, the slightly lower values of 2θ in our case for thin (<10 nm) HZO films correspond to the compressive strain stabilized rhombohedral phase. This can be understood by the fact that with decreasing HZO film thickness (below 10 nm), the d-spacing for (111) planes gradually increases (see upper inset), which thereby suggests that the in-plane compressive strain increases with reducing film thickness.^[15] The presence of the diffraction fringes around the (001) LSMO and (111) HZO reflections demonstrate high quality interfaces of the deposited films. An additional peak around 34.5° for 18 nm thin film indicates the appearance of the monoclinic phase of HZO with increasing film thickness. The epitaxial growth of the HZO/LSMO bilayer is further corroborated by TEM imaging (see Figure S1d, Supporting Information).

To improve the SNR of FTJ devices, the reduction of the ferroelectric barrier thickness down to 1 nm is needed. Therefore, stabilizing ferroelectricity in such a thickness range is the first step. The ferroelectric properties were probed by utilizing a piezoresponse force microscopy (PFM) setup. The tip was first biased with ± 4 V to write a box-in-box pattern and subsequently, the phase-contrast PFM image was obtained at 100 mV tip bias. Figure 2a shows the out-of-plane (OOP) phase contrast image of an ≈ 1 nm HZO film grown on an LSMO//STO substrate. The nearly 180° contrast difference between the outer and inner boxes indicates bistable remanent polarization states. Figure 2b shows the corresponding amplitude image of the sample. The signal at the domain walls is almost zero, which suggests the charging effects are low and thus provides further evidence of the ferroelectric character of the film. The uniform phase contrast of the unpoled and inner poled box regions demonstrates that the film is spontaneously polarized without any field cycling. Typically, few thousands of field cycling is required to “wake up” the ferroelectricity in doped HfO_2 films.^[14] Recently Cheema,^[23] have also reported the ferroelectricity in ≈ 1 nm HZO films grown on a silicon substrate by stabilizing the polar O-phase via strain imposed through the confinement of the film with a metallic capping layer; here, we have stabilized the ferroelectricity in the compressive strain induced rhombohedral phase of HZO.

Further, the robust ferroelectricity with hysteretic behavior is demonstrated by the local PFM switching on the bare HZO surface with ≈ 1 nm (Figure 2c) and ≈ 2.5 nm (Figure 2d) thick films. The SNR improved with ≈ 2.5 nm film and hence a clear hysteresis was observed in the phase signal with a corresponding butterfly-shape amplitude (d33) loop. The coercive voltages ($|V_C|$) extracted from piezo loops are ≈ 1.2 and ≈ 2.3 V for ≈ 1 and ≈ 2.5 nm films, respectively. The ferroelectric switching in ≈ 1 nm HZO film is not as sharp as we see in the case of ≈ 2.5 nm films. Further, the ferroelectric properties of HZO films were obtained through typical polarization versus voltage and positive-up-negative-down measurements (see Figure S2, Supporting Information). The remanent polarization for ≈ 2.5 nm HZO films is around $30 \mu\text{C cm}^{-2}$, which is within the range of the highest reported remanent polarization values

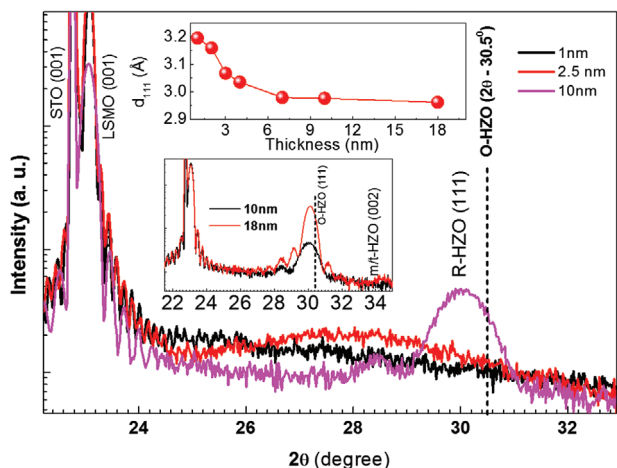


Figure 1. X-ray diffraction (θ - 2θ) patterns of $\text{Hf}_{0.5}\text{Zr}_{0.5}\text{O}_2$ (1, 2.5, and 10 nm)/ $\text{La}_{0.7}\text{Sr}_{0.3}\text{MnO}_3$ (60 nm) bilayer films, grown on a SrTiO_3 (001) substrate. The upper inset shows the variation of d-spacing for the 111-reflection of HZO with varying film thicknesses. The lower inset emphasizes the appearance of the nonpolar monoclinic phase of HZO for a 18 nm thick film.

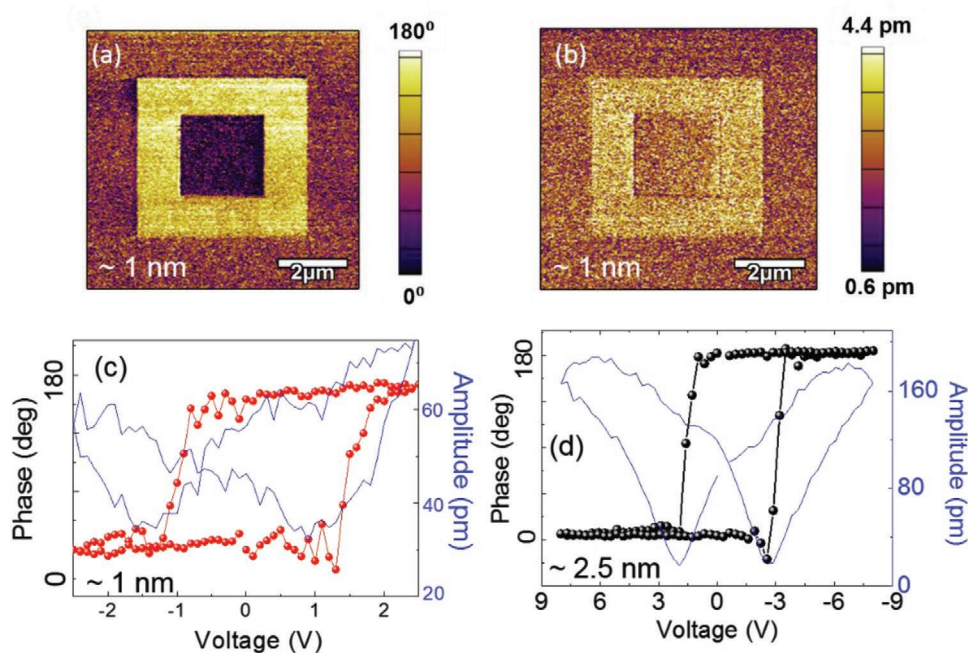


Figure 2. PFM a) phase and b) amplitude contrast images of ≈ 1 nm HZO film, and corresponding c) phase (red) and amplitude (blue) signal of the local hysteresis loop. The approximate time between the writing and reading for the PFM patterns in (a,b) is few minutes. d) The local PFM phase (black) and corresponding amplitude (blue) hysteresis loops for ≈ 2.5 nm HZO films.

for the R-HZO thin films.^[15,24] The ferroelectric property in our films is quite uniform across the sample (see Figure S2d, Supporting Information).

After achieving ferroelectricity in such ultrathin HZO films, the next step is to demonstrate the TER effect. The schematic of the patterned device structure is shown in Figure 3a. Figure 3b shows the I - V_{read} curves of an FJT device, comprising an HZO tunnel barrier ≈ 1 nm, after applying the voltage pulse of ± 2.5 V with a width of ≈ 1 ms, which is much larger than the coercive voltage of ≈ 1 nm HZO film, measured by PFM spectroscopy with a voltage pulse of ≈ 1 ms. We see a large change in the tunneling current of the device when the ferroelectric polarization direction is switched and hence, we can define the low and high tunneling current at a given voltage as the OFF and ON states, respectively. We have observed similar behavior from other devices with ≈ 1 and ≈ 2.5 nm barrier layers (see Figure S3, Supporting Information). To confirm

that the observed switching behavior in these devices is due to tunneling rather than another resistive switching mechanism, we fit the I - V data with a tunneling model (Brinkman–Dynes–Rowell model), based on Fermi–Dirac statistics and the Wentzel–Kramers–Brillouin approximation, across a rectangular shaped potential profile (for more details, see Supporting Information).^[25,26] The average barrier heights for OFF and ON states are ≈ 1.99 and ≈ 1.37 eV, respectively. The best fit was obtained with the barrier thickness of ≈ 1.3 nm for both OFF and ON states, which indicates negligible piezoelectric effect in HZO layer. Since, the piezoelectric coefficient of HZO is less than 10 pm V^{-1} ,^[27] the maximum change in the thickness of the film due to the applied electric field will be a few tens of pm, and the corresponding electroresistance will be less than 1%. The fitted value of the barrier thickness shows a good agreement with the expected value, determined by XRR and TEM analysis (see Figure S1, Supporting Information). The

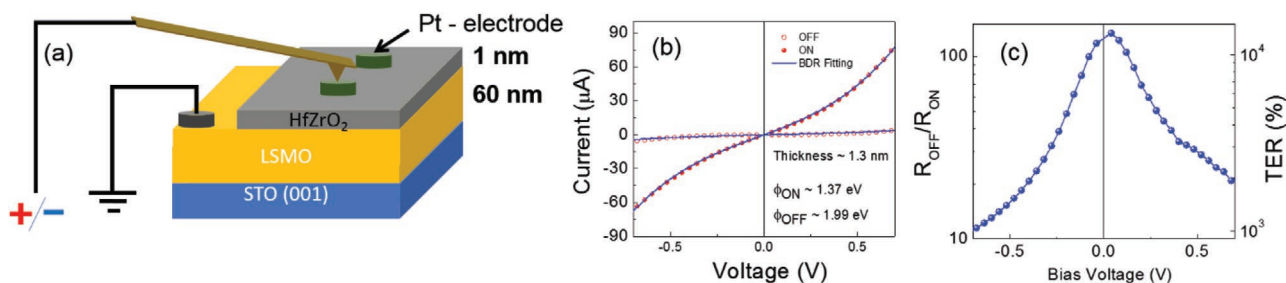


Figure 3. a) Schematic setup for the tunneling transport measurements of the ultrathin HZO tunnel devices. b) Current–voltage characteristic of a circular device ($\varnothing \approx 5 \mu\text{m}$) with $a \approx 1$ nm HZO FE tunnel barrier. Solid blue lines are the fitted results using pure direct tunneling based BDR model. c) Corresponding OFF/ON ratio (TER%) of the junction resistance with ≈ 1 nm barrier.

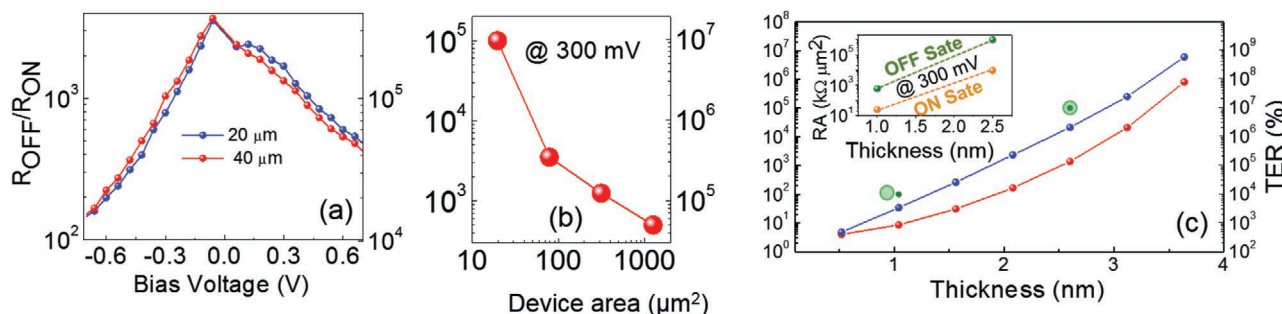


Figure 4. a) OFF/ON ratio (TER%) of a FTJ with ≈ 2.5 nm HZO barrier as a function of reading voltage for the circular devices with diameters of 20 and 40 μm . b) OFF/ON ratio (TER%) of the tunnel devices with ≈ 2.5 nm tunnel barrier as a function of the junction area. c) Calculated OFF/ON ratio (TER%) without (red) and with (blue) n-type semiconductor interface between HZO and LSMO layers, of the tunnel device with varying ferroelectric barrier thickness, using the tight-binding model. The Schottky barrier results in an increase of the electric resistance for the OFF state leading to a higher TER ratio. Experimental data (green data points) follows a theoretically predicted trend. The inset shows the RA values for the OFF and ON states of the FTJ devices increases by 2–3 orders of magnitude with changing the barrier thickness from ≈ 1 to ≈ 2.5 nm. Solid and dotted lines are guides to the eye.

OFF/ON junction resistance ratio of 135 was achieved at zero bias from a device with 1 nm thick barrier (see Figure 3c), and it gradually decreases with increasing bias voltage. Similar bias dependence of the TER effect has also been observed when the barrier thickness increases to 2.5 nm (Figure 4a). The bias voltage for one-half of the zero-bias TER for these devices was observed at 200–300 mV, which is typically considered to be an appropriate read voltage for ferroelectric tunnel devices.^[28] The ON and OFF states' resistance-area products (RA) for ≈ 1 nm barrier devices at 300 mV are ≈ 25 and ≈ 600 $\text{k}\Omega \mu\text{m}^2$, respectively which is nearly three orders of magnitude smaller than reported values for other HZO based FTJs for relatively thicker barriers.^[21] The good agreement between the switching voltages of the devices, extracted from the junction resistance versus write voltage plot (see Figure S4, Supporting Information), with the coercive voltages of the film suggests that the resistance switching in our devices is predominantly due to the ferroelectric polarization switching of the HZO barrier layer. The OFF/ON ratio of the junction resistance for the FTJ devices with 2.5 nm barrier, measured at 300 mV after the ferroelectric polarization switching at ± 4 V, increases significantly to 10^5 (TER ratio $\approx 10^7\%$) and decreases with device area (see Figure 4b). This indicates that, with reducing device size, the ferroelectric polarization reversal becomes more effective and hence shows a promising trend for scalability. Reducing the devices size also minimizes the pin holes and defects in addition to the better uniformity of the barrier layer. The TER value in our devices is among the highest reported TER values in HfO₂ barrier based FTJs.^[9,29] Recently, Yingfen Wei et al.^[29] have also reported the TER value of as high as $10^6\%$ with HZO barrier-based FTJs. Such a large TER effect was attributed to the electric field control of the oxygen vacancy concentration at the HZO/LSMO interface. Moreover, besides interfacial engineering, the activation of Fowler–Norheim tunneling at higher bias and thermionic emission at higher barrier thicknesses cannot be ignored.^[28,30] The large TER values with thicker barriers might involve these modes of transport in addition to the direct tunneling but at the cost of increasing RA values. With increasing the barrier thickness from ≈ 1 to ≈ 2.5 nm, we see nearly three orders of magnitude enhancement in the RA values of our FTJs (see inset of Figure 4c).

In order to understand the origins of the experimentally observed TER effect, we employed the tight-binding model to estimate the theoretical limit of the TER effect on our devices. Figure 4c shows the OFF/ON ratio of junction resistance at zero bias as the function of the ferroelectric barrier thickness. The OFF/ON ratio of junction resistance increases faster than exponentially with the barrier thickness. In the tight binding model, the tunneling probability is proportional to $e^{-f(U)d}$, where d is the thickness of the barrier and f is the function of the averaged barrier height U in the tight binding representation.^[31] Therefore, the TER ratio is proportional to $e^{(f(U_{\text{OFF}}) - f(U_{\text{ON}}))d}$. Clearly if the averaged barrier heights were independent on the ferroelectric barrier thickness, then TER would increase exponentially with the thickness. However, the difference between U_{ON} and U_{OFF} increases with d due to larger difference between the screening potentials at the left and right interfaces (see Figure S5, Supporting Information) leading to a faster than exponential TER thickness dependence. Although our experimental data follow the same trend, the TER ratio is 2–3 orders of magnitude higher than theoretically predicted values for 100% polarization switching.

Various physical mechanisms at the interfaces between the HZO and electrodes could potentially play roles for such large value of the OFF/ON ratio in our HZO-based FTJs. The presence of oxygen vacancies at the interfaces of metal and HZO layers have been reported and thereby the possibility of the modification of the interfacial layer cannot be ignored.^[7] Thus if we assume an existence of a thin n-type semiconductor region at the interface between HZO and LSMO, the tight binding model predicts an enhancement of the OFF/ON ratio of junction resistance (Figure 4c) close to the experimental values (for details, see Figure S6, Supporting Information). Enhancement of the TER effect due to the presence of non-polar interlayer at the barrier/electrode interface in HZO-based tunnel junctions have recently been theoretically as well as experimentally realized.^[32,33]

In summary, we have demonstrated large TER effects in ultrathin HZO based FTJs with significantly lower RA product. Ferroelectricity in these films was achieved by maintaining the rhombohedral phase through the substrate-induced strain engineering, with the remanent polarization of $30 \mu\text{C cm}^{-2}$

from ≈ 2.5 nm films. The TER ratio increases exponentially with decreasing the junction area. We have observed OFF/ON junction resistance ratio as high as 10^5 with the devices of 5 μm diameter. The TER effects can be observed even when the thickness of HZO films is reduced to ≈ 1 nm with OFF/ON junction resistance ratio of ≈ 30 and the ON-state RA product of ≈ 25 $\text{k}\Omega \mu\text{m}^2$ at 300 mV. These results are promising in terms of scalability, better SNR, and OFF/ON junction resistance ratio, which has so far rarely been achieved in HfO_2 based FTJs, and therefore show the potential for high-density nonvolatile memory applications.

Experimental Section

Film Growth, Structural and Ferroelectric Characterizations: HZO (1–18 nm)/LSMO (60 nm) bilayer films were epitaxially grown on (001)-oriented SrTiO_3 single crystal substrates by PLD technique. An excimer laser ($\lambda = 248$ nm) was used with focused laser fluence of 1–1.5 J cm^{-2} to ablate the stoichiometric ceramic targets at 1 Hz repetition rate. The substrate temperature during the deposition of these oxide films was maintained at 700 $^\circ\text{C}$, while the oxygen partial pressure was 100 and 200 mTorr for HZO and LSMO films, respectively. Subsequently, the films were cooled down to room temperature under 500 mTorr oxygen pressure. A PANalytical high resolution X-ray diffractometer with Cu $K\alpha$ radiation was used to determine the crystalline quality and thicknesses of the films. PFM of the HZO thin films was performed with an atomic force microscope (Asylum Research Cypher, MFP-3D scanning probe microscope), conductive AFM probe (Nanoandmore, DT-NCHR, Watsonville, CA) with DART mode. A Radiant Technologies Precision Premier II Ferroelectric Tester was used for ferroelectric measurements.

Device Fabrication and Measurements: A polycrystalline, Pt layer (50 nm) was first deposited ex situ on the HZO/LMSO bilayer oxide films as a top electrode layer by DC magnetron sputtering, subsequently patterned it into circular electrode with varying diameter of 5–40 μm by conventional photolithography technique. The current–voltage characteristics of the fabricated FTJ devices were measured by a custom-built measurement set-up in two-point geometry with a Keithley SourceMeter 2611. FE poling (V_{write}) was achieved by applying voltages pulses higher than the switching voltage with the pulse width of 100 μs . The bias direction was defined with respect to the top Pt electrode. The TER ratio was calculated from I – V data, defined by $\frac{R_{\text{OFF}} - R_{\text{ON}}}{R_{\text{ON}}} \times 100\%$, where R_{OFF} and R_{ON} are the junction resistance for OFF and ON states, respectively.

Tight Binding Hamiltonian Model: Calculations of TER in FTJ were performed using the non-equilibrium Greens Function formalism within the tight binding Hamiltonian model.^[34] The Hamiltonian of the FTJ consists of the Hamiltonians of the left (L) and right (R) metallic electrodes, the scattering region (C) and the coupling Hamiltonian

$$H = H_L + H_R + H_C + H_{\text{cpl}} \quad (1)$$

The Hamiltonian of the leads and the scattering region included the on-site energy ε_i and the electron hopping term t_{ij} between the nearest neighbor atomic sites i and j

$$H_{L,R,C} = \sum_{i \in L,R,C} \varepsilon_i c_i^\dagger c_i + \sum_{i,j \in L,R,C} t_{ij} c_i^\dagger c_j \quad (2)$$

Here the spin indexes were omitted since a non-magnetic FTJ was considered. The scattering region was coupled to the left and right leads through the coupling Hamiltonian

$$H_{\text{cpl}} = \sum_{i \in L,R, j \in C} (t_{ij} c_i^\dagger c_j + \text{H.c.}) \quad (3)$$

whose matrix elements consist of the nearest neighbor electron hopping terms. The electron hopping parameters in all regions were set to be $t_{ij} = -1$ eV, while the on-site energies depended on the electronic structure of the barrier, lead materials, and the electrostatic potential profile affected by the ferroelectric polarization and the bias. For instance in the left electrode ($i < 0$) the on-site energy is $\varepsilon_i = \varepsilon_L + \mu_L + \frac{\sigma_s \lambda_L}{\varepsilon_0} e^{\frac{ia_0}{\lambda_L}}$, where ε_L is the on-site energy in the bulk of the left electrode and μ_L is its chemical potential. Therefore, the ferroelectric polarization resulted in the modification of ε_i close to its interface with the ferroelectric barrier by an additional term of $\frac{\sigma_s \lambda_L}{\varepsilon_0} e^{\frac{ia_0}{\lambda_L}}$, where

$$\sigma_s = \frac{P + \varepsilon_F V/d}{1 + \varepsilon'_F (\lambda_L + \lambda_R)/d} \quad (4)$$

is the surface charge, P is the ferroelectric polarization, λ_L is the screening length in the left electrode, a_0 is the lattice constant and V is the bias voltage. Similarly, the expression for the right electrode ($i > N_B$) reads $\varepsilon_i = \varepsilon_R + \mu_R - \frac{\sigma_s \lambda_R}{\varepsilon_0} e^{-(ia_0 - d)/\lambda_R}$, where $d = N_B a_0$ is the thickness of the barrier, N_B is the number of atomic monolayers in the barrier region, and μ_R and λ_R are corresponding the chemical potential and the screening length in the right electrode. Finally, the on-site energy in the scattering region varied linearly between the left and the right interfaces given by $\varepsilon_i = \varepsilon_C + \alpha i + \beta$, where $0 < i < d$. The α and β coefficients are defined same way as in ref. [34] $\alpha = \frac{\mu_R - \mu_L}{N_B} - \frac{\sigma_s (\lambda_L + \lambda_R)}{\varepsilon_0 N_B}$ and β is the potential at the left interface. The values of the onsite energy parameters equal to $\varepsilon_L = 0$ eV, $\varepsilon_R = 2$ eV, and $\varepsilon_B = 7$ eV corresponding to Pt/HZO/LSMO FTJ were chosen. $P = 35 \mu\text{C cm}^{-2}$, $\varepsilon'_F = \frac{\varepsilon_F}{\varepsilon_0} = 22$, $\lambda_L = 0.1 \text{ \AA}$, $\lambda_R = 4.0 \text{ \AA}$, and $a_0 = 5.2 \text{ \AA}$ were also set up.

Supporting Information

Supporting Information is available from the Wiley Online Library or from the author.

Acknowledgements

The work at UC Berkeley was supported by the SRC ASCENT Center, which is one of the DARPA JUMP Centers.

Conflict of Interest

The authors declare no conflict of interest.

Data Availability Statement

Research data are not shared.

Keywords

ferroelectric materials, ferroelectric tunnel junctions, non-volatile memories, tunnel electroresistance effect

Received: November 4, 2020

Revised: March 26, 2021

Published online: May 13, 2021

- [1] S. Manipatruni, D. E. Nikonov, I. A. Young, *Nat. Phys.* **2018**, *14*, 338.
- [2] H. S. P. Wong, S. Salahuddin, *Nat. Nanotechnol.* **2015**, *10*, 191.
- [3] B. Prasad, Y. L. Huang, R. V. Chopdekar, Z. Chen, J. Steffes, S. Das, Q. Li, M. Yang, C. C. Lin, T. Gosavi, D. E. Nikonov, Z. Q. Qiu, L. W. Martin, B. D. Huey, I. Young, J. Íñiguez, S. Manipatruni, R. Ramesh, *Adv. Mater.* **2020**, *32*, 2001943.
- [4] S. Manipatruni, D. E. Nikonov, C.-C. Lin, T. A. Gosavi, H. Liu, B. Prasad, Y.-L. Huang, E. Bonturim, R. Ramesh, I. A. Young, *Nature* **2019**, *565*, 35.
- [5] S. Oh, H. Hwang, I. K. Yoo, *APL Mater.* **2019**, *7*, 091109.
- [6] N. A. Spaldin, R. Ramesh, *Nat. Mater.* **2019**, *18*, 203.
- [7] M. Mineshima, *IEEE Trans. Electron Devices* **2020**, *67*, 515.
- [8] P. Maksymovych, S. Jesse, P. Yu, R. Ramesh, A. P. Baddorf, S. V. Kalinin, *Science* **2009**, *324*, 1421.
- [9] Z. Wen, D. Wu, *Adv. Mater.* **2019**, *7*, 1904123.
- [10] R. Guo, W. Lin, X. Yan, T. Venkatesan, J. Chen, *Appl. Phys. Rev.* **2020**, *7*, 011304.
- [11] A. Chanthbouala, V. Garcia, R. O. Cherifi, K. Bouzehouane, S. Fusil, X. Moya, S. Xavier, H. Yamada, C. Deranlot, N. D. Mathur, M. Bibes, A. Barthélémy, J. Grollier, *Nat. Mater.* **2012**, *11*, 860.
- [12] V. Garcia, S. Fusil, K. Bouzehouane, S. Enouz-Vedrenne, N. D. Mathur, A. Barthélémy, M. Bibes, *Nature* **2009**, *460*, 81.
- [13] T. S. Böske, J. Müller, D. Bräuhaus, U. Schröder, U. Böttger, *Appl. Phys. Lett.* **2011**, *99*, 112901.
- [14] M. H. Park, Y. H. Lee, T. Mikolajick, U. Schroeder, C. S. Hwang, *MRS Commun.* **2018**, *8*, 795.
- [15] Y. Wei, P. Nukala, M. Salverda, S. Matzen, H. J. Zhao, J. Momand, A. S. Everhardt, G. Agnus, G. R. Blake, P. Lecoeur, B. J. Kooi, J. Íñiguez, B. Dkhil, B. Noheda, *Nat. Mater.* **2018**, *17*, 1095.
- [16] J. Lyu, I. Fina, J. Fontcuberta, F. Sánchez, *ACS Appl. Mater. Interfaces* **2019**, *11*, 6224.
- [17] M. Hoffmann, F. P. G. Fengler, M. Herzig, T. Mittmann, B. Max, U. Schroeder, R. Negrea, P. Lucian, S. Slesazek, T. Mikolajick, *Nature* **2019**, *565*, 464.
- [18] Z. Chen, Z. Chen, C. Y. Kuo, Y. Tang, L. R. Dedon, Q. Li, L. Zhang, C. Klewe, Y. L. Huang, B. Prasad, A. Farhan, M. Yang, J. D. Clarkson, S. Das, S. Manipatruni, A. Tanaka, P. Shafer, E. Arenholz, A. Scholl, Y. H. Chu, Z. Q. Qiu, Z. Hu, L. H. Tjeng, R. Ramesh, L. W. Wang, L. W. Martin, *Nat. Commun.* **2018**, *9*, 3764.
- [19] F. Ambriz-Vargas, G. Kolhatkar, R. Thomas, R. Nouar, A. Sarkissian, C. Gomez-Yáñez, M. A. Gauthier, A. Ruediger, *Appl. Phys. Lett.* **2017**, *110*, 093106.
- [20] X. Tian, A. Toriumi, *Proc. EDTM*, IEEE, Piscataway, NJ **2017**, p. 63.
- [21] Y. Wei, S. Matzen, T. Maroutian, G. Agnus, M. Salverda, P. Nukala, Q. Chen, J. Ye, P. Lecoeur, B. Noheda, *Phys. Rev. Appl.* **2019**, *12*, 031001.
- [22] F. Ambriz-Vargas, G. Kolhatkar, M. Broyer, A. Hadj-Youssef, R. Nouar, A. Sarkissian, R. Thomas, C. Gomez-Yáñez, M. A. Gauthier, A. Ruediger, *ACS Appl. Mater. Interfaces* **2017**, *9*, 13262.
- [23] S. S. Cheema, D. Kwon, N. Shanker, R. dos Reis, S.-L. Hsu, J. Xiao, H. Zhang, R. Wagner, A. Datar, M. R. McCarter, C. R. Serrao, A. K. Yadav, G. Karbasian, C.-H. Hsu, A. J. Tan, L.-C. Wang, V. Thakare, X. Zhang, A. Mehta, E. Karapetrova, R. V. Chopdekar, P. Shafer, E. Arenholz, C. Hu, R. Proksch, R. Ramesh, J. Ciston, S. Salahuddin, *Nature* **2020**, *580*, 478.
- [24] S. J. Kim, D. Narayan, J. G. Lee, J. Mohan, J. S. Lee, J. Lee, H. S. Kim, Y. C. Byun, A. T. Lucero, C. D. Young, S. R. Summerfelt, T. San, L. Colombo, J. Kim, *Appl. Phys. Lett.* **2017**, *111*, 242901.
- [25] W. F. Brinkman, R. C. Dynes, J. M. Rowell, *J. Appl. Phys.* **1970**, *41*, 1915.
- [26] D. Barrionuevo, L. Zhang, N. Ortega, A. Sokolov, A. Kumar, J. F. Scott, R. S. Katiyar, *Integr. Ferroelectr.* **2016**, *174*, 174.
- [27] S. Starschich, T. Schenk, U. Schroeder, U. Boettger, *Appl. Phys. Lett.* **2017**, *110*, 182905.
- [28] V. Garcia, M. Bibes, *Nat. Commun.* **2014**, *5*, 4289.
- [29] Y. Wei, S. Matzen, C. P. Quinteros, T. Maroutian, G. Agnus, P. Lecoeur, B. Noheda, *npj Quantum Mater.* **2019**, *4*, 62.
- [30] H. Y. Yoong, H. Wu, J. Zhao, H. Wang, R. Guo, J. Xiao, B. Zhang, P. Yang, S. J. Pennycook, N. Deng, X. Yan, J. Chen, *Adv. Funct. Mater.* **2018**, *28*, 1806037.
- [31] E. N. Economou, *Green's Functions in Quantum Physics*, Springer-Verlag, Berlin **1983**.
- [32] C. Richter, T. Schenk, M. H. Park, F. A. Tscharrntke, E. D. Grimley, J. M. LeBeau, C. Zhou, C. M. Fancher, J. L. Jones, T. Mikolajick, U. Schroeder, *Adv. Electron. Mater.* **2017**, *3*, 1700131.
- [33] Y. Goh, S. Jeon, *Appl. Phys. Lett.* **2018**, *113*, 052905.
- [34] A. Useinov, A. Kalitsov, J. Velez, N. Kioussis, *Phys. Rev. B: Condens. Matter Mater. Phys.* **2015**, *91*, 094408.